PAPER

Metallized compliant 3D microstructures for dry contact thermal conductance enhancement

IOP Publishing Journal of Micromechanics and Microengineering
J. Micromech. Microeng. **28** (2018) 055005 (7pp) https://doi.org/10.1088/1361-6439/aaaf2e

Metallized compliant 3D microstructures for dry contact thermal conductance enhancement

Jin Cui, Jicheng Wang, Yang Zhong, Liang Pan and Justin A Weibel

School of Mechanical Engineering, Purdue University, West Lafayette, IN 47907, United States of America

E-mail: liangpan@purdue.edu and jaweibel@purdue.edu

Received 20 November 2017, revised 20 January 2018
Accepted for publication 14 February 2018
Published 6 March 2018

Abstract

Microstructured three-dimensional (3D) materials can be engineered to enable new capabilities for various engineering applications; however, microfabrication of large 3D structures is typically expensive due to the conventional top-down fabrication scheme. Herein we demonstrated the use of projection micro-stereolithography and electrodeposition as cost-effective and high-throughput methods to fabricate compliant 3D microstructures as a thermal interface material (TIM). This novel TIM structure consists of an array of metallized micro-springs designed to enhance the dry contact thermal conductance between nonflat surfaces under low interface pressures (10s–100s kPa). Mechanical compliance and thermal resistance measurements confirm that this dry contact TIM can achieve conformal contact between mating surfaces with a nonflatness of approximately 5 μm under low interface pressures.

Keywords: projection micro-stereolithography, thermal interface materials, additive manufacturing, microfabrication, metallization, compliant materials

(Some figures may appear in colour only in the online journal)

1. Introduction

Micro- and nano-scale structured materials can provide unique, unintuitive combinations of properties and functions that do not exist in nature, such as materials with ultra-light weight and high stiffness [1, 2], metals with extraordinary optical responses [3, 4], and polymers with extremely high thermal conductivity [5, 6]. Many applications can utilize these engineered materials to address their dilemmas otherwise impossible with natural materials. The trend of increasing power density of electronic devices calls for new thermal management technologies in order to maintain devices at reliable operating temperatures [7–9]. One potential application for theses micro- and nano-scale structured materials includes thermal interface materials (TIMs) for enhanced dry contact thermal conductance across interfaces between mating solids. Dry contact interfaces usually have large thermal resistances because small-scale surface asperities and nonflatness severely reduce the solid-to-solid contact area available for heat flow [10, 11]; these interfacial thermal resistances contribute a major percentage of the overall resistance to heat removal from electronic packages. High contact pressures on the order of 1–100 MPa can deform the interface roughness and therefore effectively reduce dry contact thermal resistance [12, 13], but these solutions are often unpractical for fragile, flexible, or nonflat surfaces. For example, pluggable opto-electronic transceivers [14] only allow for contact pressures significantly below 1 MPa. In addition, the heat-generating components in some devices must repeatedly slide or clamp into contact with a heat sink and also disallow the use of wet TIMs such as greases and pastes. Other dry contacts, such as those operating in vacuum, have additional demands for interface robustness against contamination and outgassing.

There have been multiple promising demonstrations of nanostructured dry TIMs that conform to microscale roughness on flat interfaces [15–17]. For example, high-axial-thermal conductivity [18, 19] carbon nanotubes (CNTs) can be vertically aligned and bonded between the substrates

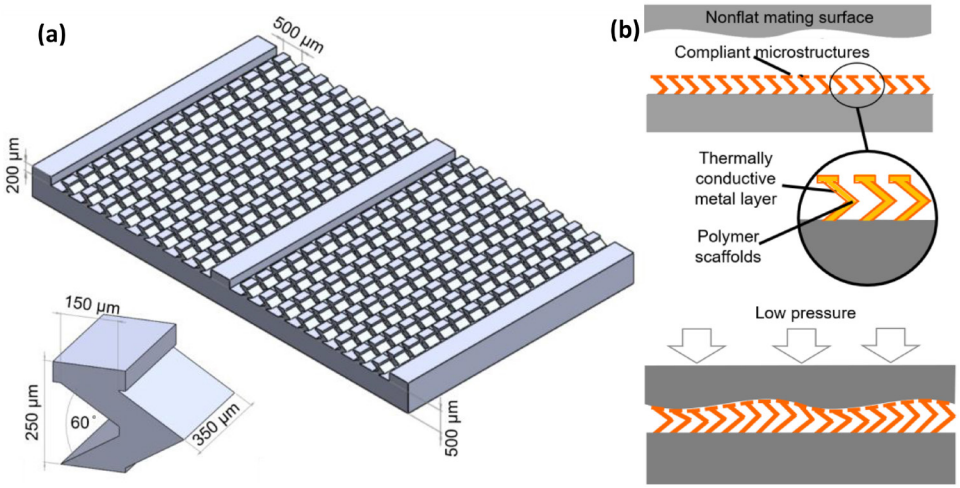

Figure 1. (a) Three-dimensional (3D) drawings of the microstructured thermal interface material (TIM) consisting of a microspring array (with inset dimensioned drawing of an individual zig zag spring element) and (b) schematic illustration of the mechanism by which a compliant microstructured TIM conforms to a nonflat surface.

[20, 21] to achieve high thermal conductance. Others also explored the use of nanoscale metallic springs fabricated with glancing angle deposition, soldered on both ends to each substrate [22, 23]. Despite their high thermal performances for contact between flat surfaces, fabrication of these nanostructured TIMs have processes that require long production times and high material consumption that cannot be economically extended for coverage over large surfaces; in addition, they often require semi-permanent bonding between surfaces. While metal surfaces can often be trivially polished to reduce the intrinsic roughness, dry TIM solutions are needed to address larger scale ~5–10 μm surface nonflatness.

The desired combination of high thermal conductance and high mechanical compliance can be achieved using metallic microspring arrays, however there is a need for suitable fabrication processes to create these structures at both sufficiently high feature fineness and low process and material costs. Previously, we presented a low-cost MEMS fabrication process to fabricate compliant polymer microspring arrays [24] using projection micro-stereolithography (μSL). The μSL technique is a fast additive fabrication process that has been used to fabricate 3D structures for a variety of biomaterial, photonic, energy storage and metamaterial applications [25–29]. In projection μSL, 3D structures are additively fabricated by stacking 2D patterns layer-by-layer, with a high resolution down to several micrometers [25, 29, 30], and as low as even 0.6 μm [31]. By using projection, this technique provides faster build speeds, higher throughput [25, 26, 30, 31] and less stitching error compared with other point-scanning type 3D microfabrication processes, such as laser selective sintering and two-photon stereolithography [32, 33]. While the fabricated polymer microspring arrays of our previous work [24] demonstrated sufficient deformation under low contact pressure so as to increase the interfacial contact area between nonflat surfaces, they had intrinsically low thermal conductivity. In this paper, we combine the cost-effective techniques of projection μSL and electrodeposition to create a new kind of metallized microstructured dry TIM to join nonflat surfaces (e.g. 5 μm nonflatness) at low (10s–100s kPa) interfacial contact pressure. Projection μSL is used to create 3D polymer scaffolds; electrodeposition is used to conformally coat the polymer scaffolds with a continuous layer of thermally conductive metal using a solution-based process. The final structure is an array of spring-like metallized microstructures which provide both high mechanical compliance and a continuous pathway for heat flow. Mechanical compliance of this microstructured dry TIM is characterized by measuring the deformation as a function of contact pressure. Compared to bare metal contact, thermal measurements are performed to demonstrate the consistency of thermal resistance yielded by this microstructured TIM under dry contact between polished metal surfaces with different nonflatness.

2. Materials and methods

2.1. Microstructure design

Figure 1(a) shows 3D drawings of the TIM design, composed of a periodic array of individual microspring elements. The zig zag spring geometry can provide high mechanical compliance suitable for different applications with low (10s–100s kPa) interfacial contact pressures. The zig zag microspring element has an overall height of 250 μm, with other characteristic dimensions labeled in figure 1(a). There are solid ribs embedded within the array, which are 50 μm shorter than the microsprings, that serve to protect the springs from overcompression when subjected to high contact pressures over the working limit. A 500 μm thick base layer is fabricated under structures in this demonstration only for ease of sample handling and transfer between substrates; in applications this base would be thinned or removed entirely by fabricating directly on the target substrate. The total footprint area of the microspring array is 6 mm $\times$ 10 mm. As shown schematically in figure 1(b), the microsprings are intended to deform and conformally contact a nonflat surface, such that there is a significant increase in the interfacial contact area compared to

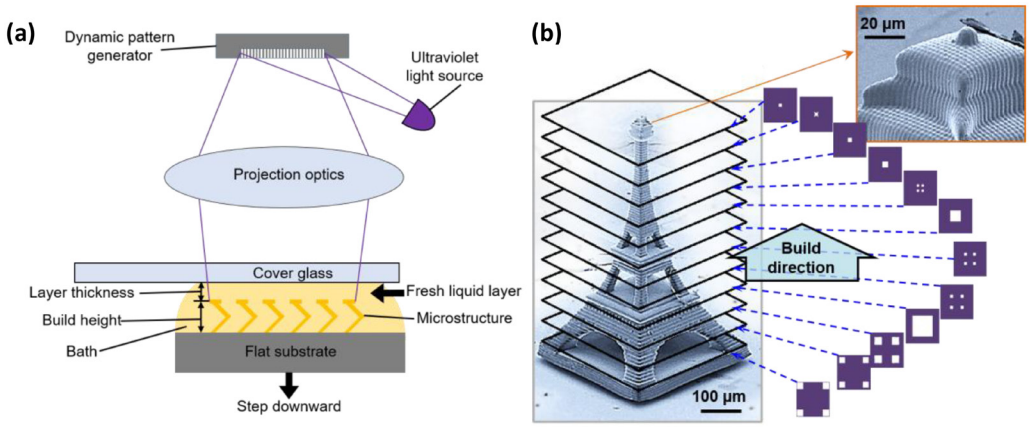

Figure 2. (a) Schematic diagram of the additive microfabrication process using projection micro-stereolithography (μSL). A dynamic pattern generator and projection optics fabricate stacked layers in an ultraviolet (UV)-curable resin bath to form the 3D microstructure. (b) Scanning electron microscope (SEM) image of a 2 mm tall Eiffel Tower structure fabricated by the μSL system. This structure is fabricated by stacking 2D cross-section patterns layer-by-layer. The inset is an enlarged view of the top of the Eiffel Tower.

bare surface-to-surface contact. The polymer microstructures must be coated with a layer of highly conductive metal to reduce the thermal resistance across the springs themselves.

2.2. Fabrication of polymer scaffolds

The projection micro-stereolithography system used herein is an in-house tool that can directly write 3D microstructures inside a liquid bath of photocurable resin at a growth speed of ~10–100 μm s^{-1} over a 1 cm^2 footprint area. The projection μSL process can operate with different kinds of photocurable resins; the microstructures in this work are fabricated using a resin consisting of a mixture of polyethylene glycol diacrylate monomer (PEGDA, Sigma-Aldrich), 2 wt% photoinitiators (Ciba, Irgacure 918), and 0.5 wt% photoabsorbers (Sudan I, Sigma-Aldrich). Under irradiation by ultraviolet (UV) light, the photoinitiator generates radicals to trigger the polymerization of PEGDA monomers. The photoabsorber limits the penetration depth of UV light into the resin bath.

The μSL system, as schematically illustrated in figure 2(a), uses an ultraviolet projection system with a programmable digital micromirror device (DMD) to dynamically cast a 1920 × 1080 pixel image to photo-define solid structures. The μSL fabrication sequence is as follows. A flat silicon substrate is initially immersed in the photocurable resin bath, with a thin layer of resin liquid covering its surface. This thin liquid layer serves as the build layer thickness used to fabricate the 3D microstructures by sequentially stacking a series of predefined 2D structures layer-by-layer. At each building step, one UV image irradiates the top layer of the photocurable resin. After polymerization of the exposed layer, the UV irradiation is switched off and a mechanical stage is moved downward to allow a fresh layer of uncured resin to flow over top of the previously solidified plane to form the next build layer. The DMD image changes to the next pattern and the process cycle of irradiation, polymerization, and recoating repeats until the entire 3D structure is fabricated. After fabrication, the 3D microstructures are removed from the resin bath and rinsed with isopropyl alcohol and acetone to remove uncured resin. Figure 2(b) shows a scanning electron microscope (SEM) image of a 2 mm tall Eiffel Tower structure fabricated using this μSL system. Before fabrication, a 3D model of the structure is sliced into a stack of 2D cross-section images as illustrated. The build layer thickness increments of 20 μm can be observed from the aliased geometric features on the sidewalls of the tower. The grid-patterned line textures observed in the inset view of the tower peak correspond to the pixels of the DMD, which indicate that the resolution of the system is better than 10 μm.

2.3. Metallization of polymer scaffolds

The polymer microsprings are metallized in two sequential steps: nickel electroless plating and copper electroplating. For the nickel electroless plating, the polymer sample is first etched in a 0.25 wt% potassium permanganate ($KMnO_4$, Sigma-Aldrich) aqueous solution at 80 °C to form small holes on the surface for anchoring of the metal layer. The structure is then sensitized in a 1 wt% tin (II) chloride ($SnCl_2$, Sigma-Aldrich) solution and activated in a 0.025 wt% palladium chloride ($PdCl_2$, Sigma-Aldrich) solution. The $PdCl_2$ reacts with $SnCl_2$ to generate small palladium particles on the surface that serve as a catalyst. Finally, the plating solution is 3 wt% nickel sulfate ($NiSO_4$, Sigma-Aldrich) solution with 2 wt% sodium hypophosphite (NaH_2PO_2, Sigma-Aldrich) solution as a reducing agent, 1.7 wt% sodium malate ($C_4H_4Na_2O_5$, Sigma-Aldrich) solution as complexing agent, and 0.9 wt% acetic acid to adjust the pH value to 4–5. The coated nickel layer serves as an electrically conductive based material for the subsequent copper electroplating.

For the copper electroplating process, a copper sheet (99.9% purity) is used as the anode and the nickel-coated microstructure as the cathode; 22.5 wt% copper (II) sulfate ($CuSO_4$, Sigma-Aldrich) aqueous solution is used as the electrolyte. During the pulsed electroplating process, an electrical current source generates a 1 Hz square waveform at a 64 mA peak current. This pulsed electroplating can provide better coating uniformity and attachment compared to a constant

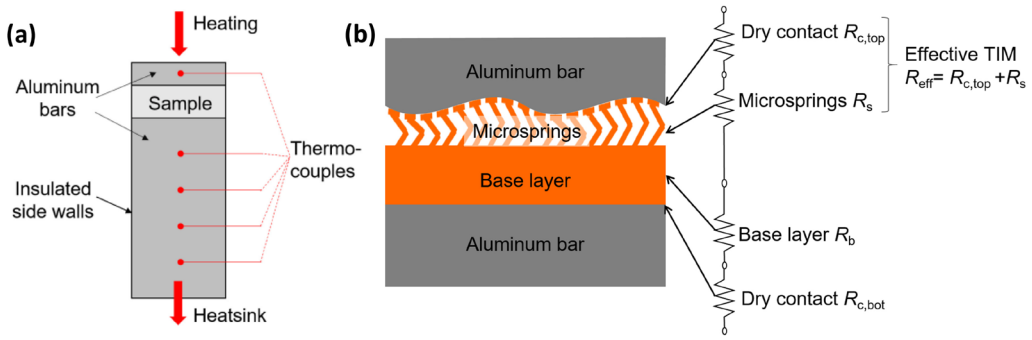

Figure 3. (a) Schematic diagram of thermal resistance measurement using 1D reference bars and (b) illustration of the component resistances contributing to the total thermal resistance measured in the test facility.

current. The thickness of this copper (thermal conductivity ~400 $W{\cdot}m^{-1}{\cdot}K^{-1}$) layer is controlled by adjusting the plating duration.

2.4. Experimental measurements of mechanical compliance and thermal resistance

The mechanical compliance of the fabricated microstructures is evaluated using an in-house test facility. To perform the tests, a fabricated sample is placed between two rigid, parallel surfaces. The bottom surface is a fixed platform positioned by a three-axis translation stage. The top surface plate is used to gently apply a normal compression onto the sample using a variable-force loading stage. The total force applied to sample is measured using a factory-calibrated load cell (Omega LCM305; $\pm$ 0.25 N). Meanwhile, the vertical displacement of the top plate during compression is measured using a digital camera that views the side of sample stack-up using high-magnification zoom lens (Keyence VH-Z50L); the displacement can be resolved to within the pixel size of 0.6 μm. At each fixed load, a static image is acquired using the camera and the force is recorded using the data acquisition system. The load force is successively increased and decreased two times to obtain a set of loading and unloading curves that captures any hysteresis during sample deformation.

A schematic diagram of thermal resistance measurement system is shown in figure 3(a). The facility is designed to measure the overall thermal resistance between the mating surfaces of the upper and lower bars (6061 aluminum, thermal conductivity 150 $W{\cdot}m^{-1}{\cdot}K^{-1}$). The sample is placed between these two bars, which have the same cross-sectional area and serve as one-dimensional (1D) heat conduction pathways. A serpentine resistance heating wire is attached to the top bar as heat source and a pin fin heatsink is used to reject heat to the environment through the lower bar. A thick thermal insulation layer (not shown in the figure) made of polyetheretherketone (PEEK, thermal conductivity ~0.3 W $m^{-1}{\cdot}K^{-1}$) is applied around the sides of the sample and aluminum bars to ensure 1D heat conduction. Five thermocouples (Omega T-type, $\pm$0.5 °C) are inserted into tapped holes to measure temperature at fixed positions ($\pm$0.5 mm) along the centerline of the bars. The temperature gradient along the rake of four thermocouples in the lower bar is used to measure heat flux passing through the bars and extrapolate the temperature at bottom of the sample; the thermocouple in the upper bar is used to measure a temperature on the opposite side of the interface. During the thermal resistance measurement, the microsprings array faces upward and directly contacts the surface of the upper aluminum bar, as shown in figure 3(b).

The effective thermal resistance of the dry TIM (R_{eff}) includes the resistance of microsprings (R_s) and the interfacial resistance between microsprings and top mating surface ($R_{c,top}$). The polymer base layer, which is used for convenience of transferring the samples between test facilities, also introduces a base resistance (R_b) and interfacial resistance between the substrate and bottom mating surface ($R_{c,bot}$); while these resistance ($R_b + R_{c,bot}$) contribute to the total thermal resistance measured in this facility, they are not considered to be a portion of the effective dry TIM resistance because in applications the microstructures would be fabricated directly onto the part surfaces.

3. Results and discussion

3.1. Polymer and metallized microspring array

Plan view microscopic pictures of the fabricated structure before and after metal plating are shown in figure 4. Figure 4(a) shows an optical plan view image of the polymer microspring array. The microspring were fabricated using a layer thickness increments of 10 μm. All of the 240 microsprings are fabricated to the same dimension without significant defects, which indicates a good fabrication uniformity throughout the whole fabrication area. After electroless nickel plating (figure 4(b)), the nickel (thermal conductivity ~50 $W{\cdot}m^{-1}{\cdot}K^{-1}$) layer is shiny and has a uniform thickness of ~2 μm (as measured via inspection using a high-resolution optical microscope). After copper electroplating, the nickel-coated structures become uniformly covered by a 10 μm thick copper layer (figure 4(c)). Side-view microscope and SEM images of the copper coated structure are respectively shown in figures 4(d) and (e). Note that the surface of the copper layer is rough compared to the nickel layer underneath.

3.2. Mechanical compliance

The mechanical compliance of the microspring array is evaluated at three different coating stages: bare polymer scaffolds

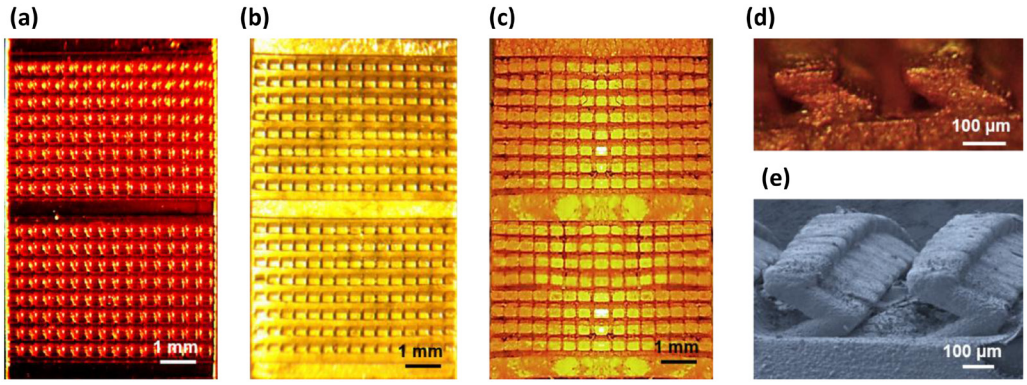

Figure 4. Plan view microscope pictures of microspring array: (a) polymer scaffold, (b) after nickel coating, and (c) after copper coating. High-magnification side view (d) microscope and (e) SEM images of the final copper-coated microspring structure.

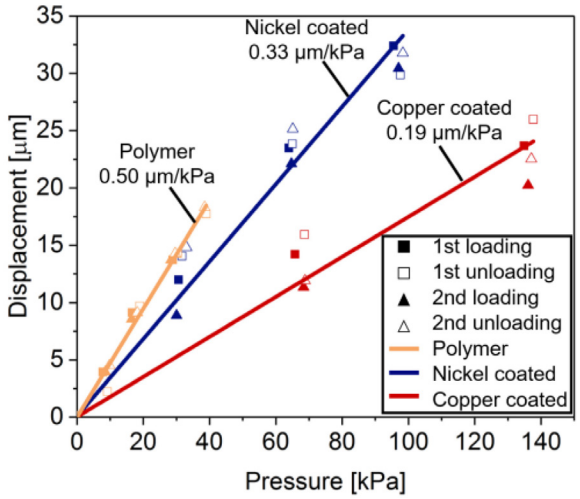

Figure 5. Characterization of the displacement as a function of the applied pressure of the polymer, nickel-coated, and copper-coated structures: the solid symbols indicate loading direction and open symbols unloading; squares indicate the first loading cycle and triangles the second cycle. Solid lines are the linear fits of the data. The slopes of best linear fit solid lines indicate mechanical compliance of the microspring arrays.

(i.e. no coating), after nickel coating, and after copper coating. The structures were each loaded up to a maximum deformation of approximately 35 μm (14% of the structure height). Figure 5 plots the measured vertical displacement of the top plate compressing the structures as a function of the applied pressure for two loading and unloading cycles each. The deformation behavior of the structures is linear, elastic, and have no hysteresis over the ranges of applied pressures. Given the good linearity of the measured displacement versus pressure, the mechanical compliances can be accurately extracted using a linear fit of the data. The compliances of the bare polymer, nickel-coated and copper-coated microspring arrays are 0.50, 0.33, and 0.19 μm kPa^{-1}, respectively, with uncertainties of ~5% of the measured values. The uncertainty of the mechanical compliance is calculated from the root measurement uncertainties of force ($\pm$0.25 N) and displacement ($\pm$3 pixels, i.e. $\pm$1.8 μm). Although the measured compliance decreases after metal plating, the compliance of the copper-coated microspring array is still predicted to be more than three orders of magnitudes better than that of pure metal microsprings having the same geometry based on a simplified beam-bending model where the two arms of the zig zag microspring are treated as cantilevers. Having this compliance, the copper-coated dry TIM should conform to surfaces with nonflatness on the order of 5 μm at ~25 kPa.

3.3. Thermal resistance

The thermal resistances of these microstructured dry TIMs are evaluated for both polished flat and polished nonflat mating surfaces. The sample thermal resistance is measured under a contact pressure of 300 kPa, such that the curvature in the base layer, caused by residual stress after metallization, can be flattened. At this pressure, the microsprings are in a maximally compressed state down to the protective ribs. The microsprings have no visible deformation and can recover to the original shape and dimension after being compressed under pressures of ~300 kPa. For the flat mating surface, the thermal resistances of structures are evaluated for the three configurations of bare polymer, nickel coated, and copper coated, to understand the effect of the metallization. Figure 6(a) shows the measured thermal resistances of three different structures (bare polymer, nickel coated, and copper coated) mated to a polished flat surface. The bare polymer structures have the highest total thermal resistance of 81 $\pm$ 31 cm^2·K W^{-1}. Due to the addition of the high-thermal-conductivity metal layers, the nickel- and copper-coated samples have lowered resistances of 42 $\pm$ 13 and 28 $\pm$ 7 cm^2·K W^{-1}, respectively.

Figure 6(a) shows the contributing resistances (as defined in figure 3(b)) which are determined through control experiments and analysis. The polymer-to-metal dry contact thermal resistance ($R_{c,bot}$) is measured to be 11.8 cm^2·K W^{-1} at the contact pressure of 300 kPa based on separate experiments in which a solid polymer block is inserted into the interface. From the same control experiment, the thermal resistance of the polymer material at this base thickness (R_b) is measured to be 4.2 cm^2·K W^{-1}. These $R_{c,bot}$ and R_b values are identical for all three configurations. The remaining portion of the total thermal resistance corresponds to the effective thermal resistances of the microstructured dry

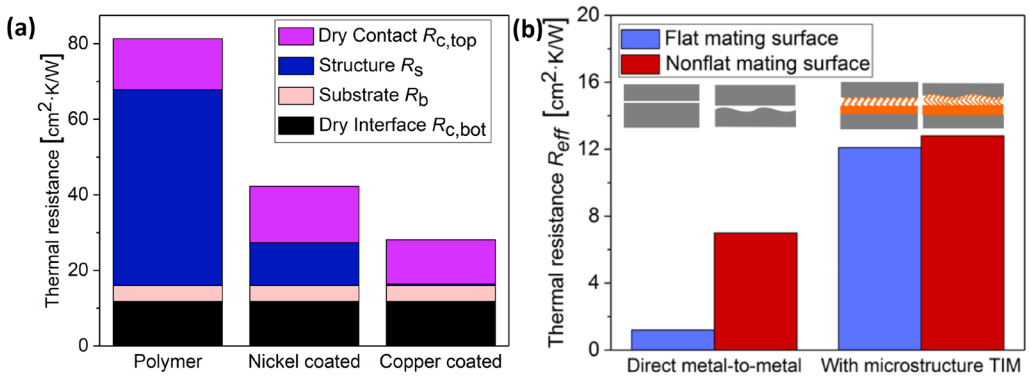

Figure 6. (a) Thermal resistances of the microstructured dry TIM having polymer, nickel-coated, and copper-coated microsprings (flat mating interface); (b) comparison of effective thermal resistances for flat and non-flat mating interfaces with the copper-coated microstructured dry TIM and without (i.e. direct metal-to-metal).

TIMs (R_{eff}), which correspond to 65.3, 26.3 and 12.1 $cm^2 \cdot K\ W^{-1}$ for the three coating configurations of bare polymer, nickel-coated, and copper-coated microsprings, respectively. The effective thermal resistance (R_{eff}) is reduced by 80% after metallization with copper. To further decompose the contributions to the effective thermal resistance, the thermal resistance of the three microspring structures (R_s), assuming simplified 1D heat conduction through the nominal microspring design geometry using known material properties, are calculated to be 51.8, 11.3, and 0.4 $cm^2 \cdot K\ W^{-1}$, respectively. The remaining resistance is attributed to the interfacial contributions $R_{c,top}$, which are 13.5, 15.0, and 11.7 $cm^2 \cdot K\ W^{-1}$, respectively. As expected, the interfacial contribution $R_{c,top}$ is similar for all three cases under this contact pressure, as the primary cause is the microscale roughness and asperities at the interface.

While the thermal resistance measurements made using the flat substrates allows understanding of the contributing thermal resistances, the purpose of the microstructure dry TIM is to enhance the contact conductance under conditions where there is a highly nonflat interface. To evaluate the dry TIM thermal performance under these conditions, the mating surface of the top aluminum bar is laser-etched to achieve a canonical nonflatness of 5 μm, namely, a periodic line texture (0.5 mm width, 5 μm step height, and 2 mm pitch). Thermal resistance tests are also performed for the cases of direct metal-to-metal contact. Figure 6(b) shows the effective dry thermal resistance (R_{eff}) for the cases with and without the copper-coated microstructured TIM inserted, for both the flat and nonflat surfaces. For the direct metal-to-metal contact between, the dry contact thermal resistance increases by approximately 6 times from 1.2 ± 0.7 to 7.0 ± 1.7 $cm^2 \cdot K\ W^{-1}$ when the mating surface is nonflat. For the copper-coated microstructured dry TIM, the thermal resistance only increases by ~6% from 12.1 to 12.8 $cm^2 \cdot K\ W^{-1}$ after replacing the flat mating surface with a nonflat one. While direct metal-to-metal contact has a lower absolute thermal resistance, this result provides a critical proof of concept that the dry contact thermal resistance of this compliant metallized microstructured TIM is nearly unaffected by the presence of surface nonflatness.

4. Conclusions

We report here a new low-cost, high-throughput method to fabricate a microstructured dry TIM, which can enhance the thermal contact conductance across dry interfaces with large nonflatness (5 μm) under relatively low pressures (10s–100s kPa). Projection micro-stereolithography is used to fabricate the microscale polymer spring structures designed for high compliance; this polymer scaffold is metallized to enhance the thermal conductance of the structures. This new dry TIM is demonstrated to exhibit high mechanical compliance. Furthermore, thermal resistance tests using flat and nonflat surfaces demonstrate that the effective resistance of this dry TIM is nearly unaffected by the surface nonflatness; this is in stark contrast with direct metal-to-metal interfaces that have a thermal resistance value strongly coupled with the nonflatness. This work demonstrated the possibility for designing and creating large-scale microstructured TIMs for dry contact interfaces under low pressures. Future work will focus on further enhancing the thermal performance of the microstructured dry TIMs by reducing the microscale surface roughness on the metallized layer, which was shown to be the primary contributor to the thermal resistance.

Acknowledgments

Financial support for this work was provided by members of the Cooling Technologies Research Center (CTRC), a National Science Foundation Industry/University Cooperative Research Center at Purdue University, and the National Science Foundation (grant Nos. CMMI-1554189 and CMMI-1634832). We also thank Xuemei Chen for acquiring the SEM images of the 2 mm tall Eiffel Tower, and Chen Chen for acquiring the SEM images of the copper-coated microstructure array.

ORCID iDs

Liang Pan https://orcid.org/0000-0002-6540-3957
Justin A Weibel https://orcid.org/0000-0002-2046-406X

References

[1] Schaedler T A, Jacobsen A J, Torrents A, Sorensen A E, Lian J, Greer J R, Valdevit L and Carter W B 2011 Ultralight metallic microlattices *Science* **334** 962–5

[2] Zheng X *et al* 2014 Ultralight, ultrastiff mechanical metamaterials *Science* **344** 1373–7

[3] Smith D R, Padilla W J, Vier D C, Nemat-Nasser S C and Schultz S 2000 Composite medium with simultaneously negative permeability and permittivity *Phys. Rev. Lett.* **84** 4184

[4] Shelby R A, Smith D R and Schultz S 2001 Experimental verification of a negative index of refraction *Science* **292** 77–9

[5] Veca L M, Meziani M J, Wang W, Wang X, Lu F, Zhang P, Lin Y, Fee R, Connell J W and Sun Y P 2009 Carbon nanosheets for polymeric nanocomposites with high thermal conductivity *Adv. Mater.* **21** 2088–92

[6] Shen S, Henry A, Tong J, Zheng R and Chen G 2010 Polyethylene nanofibres with very high thermal conductivities *Nat. Nanotechnol.* **5** 251–5

[7] Atluri V P *et al* 2003 Critical aspects of high-performance microprocessor packaging *MRS Bull.* **28** 21–34

[8] Garimella S V *et al* 2008 Thermal challenges in next-generation electronic systems *IEEE Trans. Compon. Packag. Technol.* **31** 801–15

[9] Prasher R 2006 Thermal interface materials: historical perspective, status, and future directions *Proc. IEEE* **94** 1571–86

[10] Cooper M G, Mikic B B and Yovanovich M M 1969 Thermal contact conductance *Int. J. Heat Mass Transfer* **12** 279–300

[11] Madhusudana C V and Ling F F 1996 *Thermal Contact Conductance* (Berlin: Springer) pp 1–43

[12] Lambert M A and Fletcher L S 1993 Review of the thermal contact conductance of junctions with metallic coatings and films *J. Thermophys. Heat Transfer* **7** 547–54

[13] Merrill C T and Garimella S V 2011 Measurement and prediction of thermal contact resistance across coated joints *Exp. Heat Transfer* **24** 179–200

[14] OIF-Thermal-01.0 2015 *Implementation Agreement for Thermal Interface Specification for Pluggable Optics Modules* (Optical Internetworking Forum)

[15] Bar-Cohen A, Matin K and Narumanchi S 2015 Nanothermal interface materials: technology review and recent results *J. Electron. Packag.* **137** 040803

[16] McNamara A J, Joshi Y and Zhang Z M 2012 Characterization of nanostructured thermal interface materials—a review *Int. J. Therm. Sci.* **62** 2–11

[17] Hansson J, Nilsson T M, Ye L and Liu J 2017 Novel nanostructured thermal interface materials: a review *Int. Mater. Rev.* **63** 22–45

[18] Iijima S 1991 Helical microtubules of graphitic carbon *Nature* **354** 56–8

[19] Marconnet A M, Panzer M A and Goodson K E 2013 Thermal conduction phenomena in carbon nanotubes and related nanostructured materials *Rev. Mod. Phys.* **85** 1295

[20] Wasniewski J R, Altman D H, Hodson S L, Fisher T S, Bulusu A, Graham S and Cola B A 2012 Characterization of metallically bonded carbon nanotube-based thermal interface materials using a high accuracy 1D steady-state technique *J. Electron. Packag.* **134** 020901

[21] Lin W, Zhang R, Moon K S and Wong C P 2010 Synthesis of high-quality vertically aligned carbon nanotubes on bulk copper substrate for thermal management *IEEE Trans. Adv. Packag.* **33** 370–6

[22] Shaddock D, Weaver S, Chasiotis I, Shah B and Zhong D 2011 Development of a compliant nanothermal interface material *ASME Int. Technical Conf. and Exhibition on Packaging and Integration of Electronic and Photonic Microsystems (InterPACK)*

[23] Kempers R, Lyons A M and Robinson A J 2014 Modeling and experimental characterization of metal microtextured thermal interface materials *J. Heat Transfer* **136** 011301

[24] Wasielewski R, Cui J, Pan L and Weibel J A 2016 Fabrication of compliant three-dimensional microstructures as surface coatings for dry contact thermal conductance enhancement *15th IEEE Intersociety Conf. on Thermal and Thermomechanical Phenomena in Electronic Systems (ITherm)* pp 134–9

[25] Choi J W, Wicker R, Lee S H, Choi K H, Ha C S and Chung I 2009 Fabrication of 3d biocompatible/biodegradable micro-scaffolds using dynamic mask projection microstereolithography *J. Mater. Process. Technol.* **209** 5494–503

[26] Zheng X, Deotte J, Alonso M P, Farquar G R, Weisgraber T H, Gemberling S, Lee H, Fang N and Spadaccini C M 2012 Design and optimization of a light-emitting diode projection micro-stereolithography three-dimensional manufacturing system *Rev. Sci. Instrum.* **83** 125001

[27] Bao Y, He C, Zhou F, Stuart C and Sun C 2012 A realistic design of three-dimensional full cloak at terahertz frequencies *Appl. Phys. Lett.* **101** 031910

[28] Lin D, Nian Q, Deng B, Jin S, Hu Y, Wang W and Cheng G J 2014 Three-dimensional printing of complex structures: man made or toward nature? *ACS Nano* **8** 9710–5

[29] Chen Q, Xu R, He Z, Zhao K and Pan L 2017 Printing 3d gel polymer electrolyte in lithium-ion microbattery using stereolithography *J. Electrochem. Soc.* **164** A1852–7

[30] Ha Y M, Choi J W and Lee S H 2008 Mass production of 3D microstructures using projection microstereolithography *J. Mech. Sci. Technol.* **22** 514

[31] Sun C, Fang N, Wu D M and Zhang X 2005 Projection micro-stereolithography using digital micro-mirror dynamic mask *Sensors Actuators* A **121** 113–20

[32] Meza L R, Das S and Greer J R 2014 Strong, lightweight, and recoverable three-dimensional ceramic nanolattices *Science* **345** 1322–6

[33] Soukoulis C M and Wegener M 2011 Past achievements and future challenges in the development of three-dimensional photonic metamaterials *Nat. Photon.* **5** 523–30